Title

Ferrobotic swarms enable accessible and adaptable automated viral testing

Authors

Lin, Haisong
Yu, Wenzhuo
A. Sabet, Kiarash
et al.

Peer reviewed

Article

Ferrobotic swarms enable accessible and adaptable automated viral testing

🔴 Check for updates

Haisong Lin[1,4], Wenzhuo Yu[1,4], Kiarash A. Sabet[1,4], Michael Bogumil[2], Yichao Zhao[1], Jacob Hambalek[2], Shuyu Lin[1], Sukantha Chandrasekaran[3], Omai Garner[3], Dino Di Carlo[2✉] & Sam Emaminejad[1,2✉]

Expanding our global testing capacity is critical to preventing and containing pandemics[1–9]. Accordingly, accessible and adaptable automated platforms that in decentralized settings perform nucleic acid amplification tests resource-efficiently are required[10–14]. Pooled testing can be extremely efficient if the pooling strategy is based on local viral prevalence[15–20]; however, it requires automation, small sample volume handling and feedback not available in current bulky, capital-intensive liquid handling technologies[21–29]. Here we use a swarm of millimetre-sized magnets as mobile robotic agents ('ferrobots') for precise and robust handling of magnetized sample droplets and high-fidelity delivery of flexible workflows based on nucleic acid amplification tests to overcome these limitations. Within a palm-sized printed circuit board-based programmable platform, we demonstrated the myriad of laboratory-equivalent operations involved in pooled testing. These operations were guided by an introduced square matrix pooled testing algorithm to identify the samples from infected patients, while maximizing the testing efficiency. We applied this automated technology for the loop-mediated isothermal amplification and detection of the SARS-CoV-2 virus in clinical samples, in which the test results completely matched those obtained off-chip. This technology is easily manufacturable and distributable, and its adoption for viral testing could lead to a 10–300-fold reduction in reagent costs (depending on the viral prevalence) and three orders of magnitude reduction in instrumentation cost. Therefore, it is a promising solution to expand our testing capacity for pandemic preparedness and to reimagine the automated clinical laboratory of the future.

Over the past two decades, major epidemics (SARS, Zika, MERS and Ebola) and pandemics (H1N1 and COVID-19) have emerged with increasingly alarming regularity[1–3]. Although currently the world is grappling with the COVID-19 pandemic, the occurrence of the next wave of infectious disease outbreaks in the coming years is deemed inevitable, given the rise in population, urbanization and global travel and/or trade. In that regard, large-scale population screening is the primary safeguard to contain epidemics, prevent pandemics and mitigate their human and economic costs on their onset[4–6].

Accordingly, increasing our viral diagnostic and surveillance testing capacity globally is fundamental to our epidemic and pandemic preparedness[7–9]. Among the test options, nucleic acid amplification tests (NAATs) are advantageous over the antigen-based and antibody-based counterparts, owing to their superior sensitivity, specificity and ability for rapid deployment without the need to generate specific diagnostic antibodies[10,11]. To perform NAATs at large scale and frequency, accessible automated testing platforms are required that can be deployed in decentralized settings to analyse samples with high

throughput, fast turnaround time and minimal capital cost and/or reagent use[12–14]. In particular, the strategic pooling of samples[15–18], when most patients are expected to be negative, can lead to a marked reduction in resource utilization amid pandemic-induced supply chain disruptions (outweighing the marginal risk of dilution-induced false negatives[19,20]). Accordingly, flexible testing workflows dictated by adaptive pooling algorithms—such as viral prevalence-based algorithms—that are intended to maximize the screening efficiency are needed (Fig. 1a,b).

However, current automated NAAT-based testing platforms are unable to perform the integrated liquid handling, analysis and automated feedback processes that are necessary to achieve these flexible workflows[21–23]. In addition, they use bulky, expensive and reagent-wasteful robotic liquid handlers and bioinstruments, with heavy installations and maintenance needs, and thus, they are restricted to centralized laboratory settings[24–29].

To enable adaptive pooled testing, here we created an automated NAAT-based testing platform, which performs programmable liquid

[1]Interconnected and Integrated Bioelectronics Lab (I²BL), Department of Electrical and Computer Engineering, UCLA, Los Angeles, CA, USA. [2]Department of Bioengineering, UCLA, Los Angeles, CA, USA. [3]Department of Pathology and Laboratory Medicine, UCLA, Los Angeles, CA, USA. [4]These authors contributed equally: Haisong Lin, Wenzhuo Yu, Kiarash A. Sabet. ✉e-mail: dicarlo@ucla.edu; emaminejad@ucla.edu
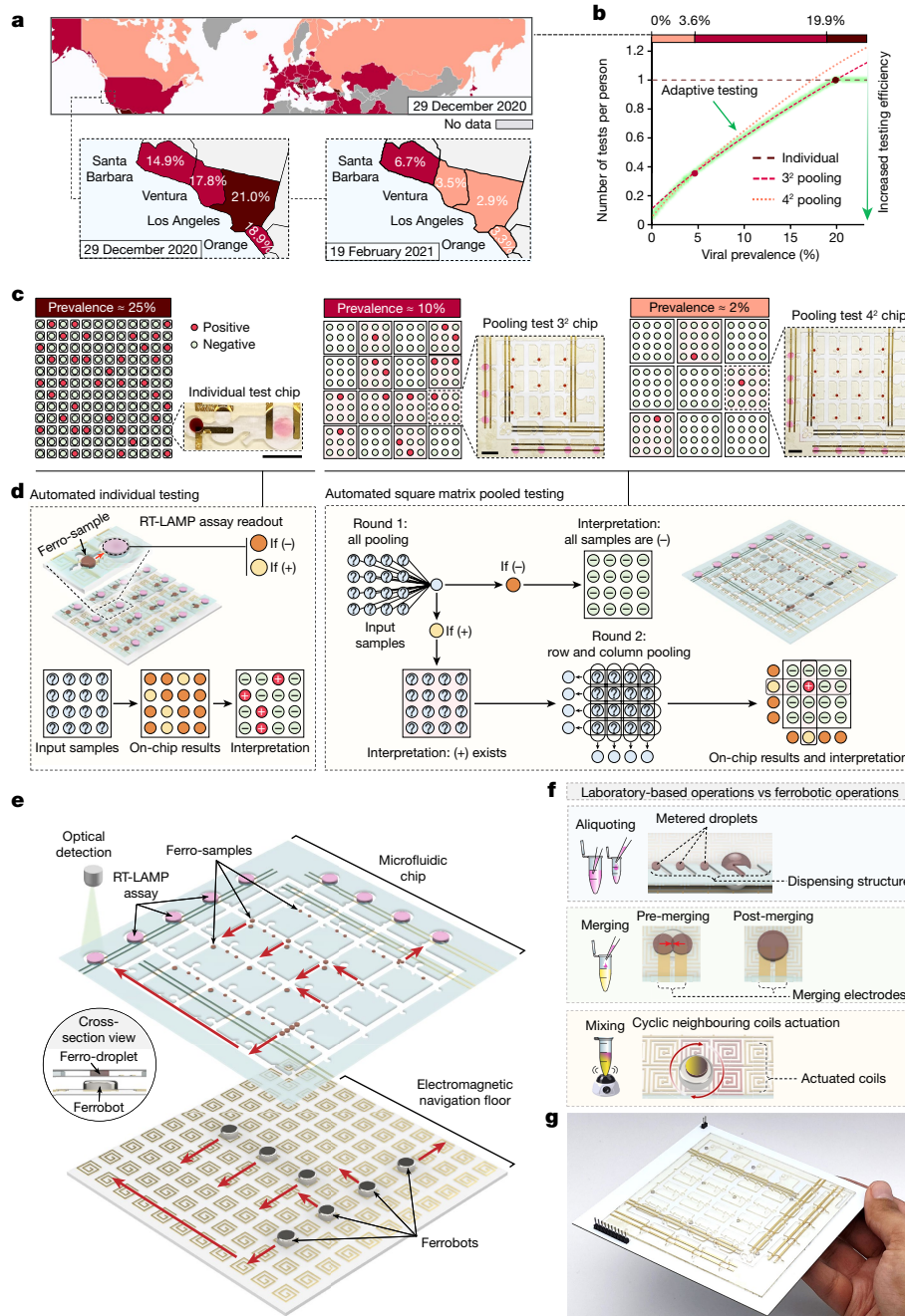
Fig. 1 | Overview of the bioanalytical swarm ferrobotic platform for accessible, adaptable and automated viral testing. a, Spatiotemporal varying COVID-19 viral prevalence (based on the test positivity rate data from Our World in Data and California Health and Human Services Open Data Portal). Map generated using Visme. **b**, The required number of tests per person to find all infected people (across different levels of local viral prevalence), based on the square matrix pooled testing strategy. The green-highlighted curve illustrates that maximal screening efficiency can be achieved via adaptive (prevalence-based) testing. **c**, Optimal testing modes and the associated

ferrobotic chips (scale bar, 1 cm) for the representative local viral prevalence levels of 25%, 10% and 2%. **d**, Overview of the automated workflows for individual and pooled testing of 16 samples. **e**, Exploded schematic of a representative ferrobotic viral testing platform (for example, 4² pooling). Red arrows, direction of the motion of the ferrobots and droplets. **f**, The ferrobotic equivalents of laboratory-based NAAT liquid handling operations, including aliquoting, merging and mixing. **g**, Optical image of a representative ferrobotic viral testing platform for 4² pooled testing.

handling and bioanalytical operations within flexible workflows and in a parallel manner. Instead of resource-intensive and functionally limited robotic liquid handlers, we used a swarm of individually addressable millimetre-sized magnets as mobile robotic agents ('ferrobots') that can manipulate magnetic nanoparticle-spiked droplets ('ferro-droplets') with high precision and robustness. The seamless integration of fluid-ware, hardware and software allowed for programming and streamlining the droplet-based operations, and delivering versatile automated

NAAT-centred workflows within a compact platform (for example, here we implemented reverse transcription loop-mediated isothermal amplification (RT-LAMP)). To maximize the screening efficiency, we formulated a prevalence-based adaptive testing algorithm (Fig. 1b and Supplementary Note 1). This algorithm particularly determines the optimal testing mode and guides the operational workflow in accordance with a square matrix pooling scheme (Fig. 1c,d), without entailing overly burdensome sample handling procedures. Adopting this approach over

Article

the fixed individual testing approach (universally pursued) allows for substantial savings over a wide viral prevalence range.

Figure 1e–g illustrates a representative ferrobotic testing platform, which consists of two modules (entirely constructed by low-cost components): (1) a disposable oil-filled microfluidic chip with passive and active actuation interfaces that hosts input samples and ferrofluid or assay reagents, and (2) a printed circuit board (PCB), featuring 2D arrayed coils ('navigation floor'), which can be independently activated to electromagnetically direct individual ferrobots.

We realized the miniaturized bioanalytical operations and workflows within the framework of ferrobotics, because it simultaneously offers high degrees of robustness, diversity, programmability and scalability for low-volume sample handling. Within this framework, we developed and characterized a suite of operations, including droplet transportation, aliquoting, merging, mixing and heating, which are key to the on-chip implementation of NAAT-based assays (Fig. 2 and Extended Data Fig. 1).

By programming the underlying PCB-based coils, we electromagnetically directed the ferrobots to carry ferro-droplets within different oil environments, in which rapid droplet transportation with a maximum velocity range of 5–50 mm s^{-1} was achieved (Fig. 2a and Extended Data Fig. 1b). We found that Novec (oil)–PicoSurf (surfactant) yielded the maximum ferro-droplet speed (owing to its low viscosity; Supplementary Note 2, Supplementary Table 5 and Supplementary Fig. 6), as well as being compatible with the RT-LAMP assay.

Figure 2b illustrates the precise and tuneable ferrobotic sample aliquoting capability in the optimized Novec oil environment. In our context, aliquoting is a critical step for precise sample metering and creating sub-samples for multiplexing and multiround pooling analysis. Aliquoting is achieved by directing a ferrobot carrying a ferro-droplet along a corrugated structural feature, which in turn causes the dispensing of a smaller ferro-droplet (as an aliquot). By adjusting the corrugation opening and/or the channel height, the volume of the aliquot could be tuned over two orders of magnitude (for example, here 100 nl to 10 μl; Extended Data Figs. 1c,d and 2a).

To realize droplet merging, we utilized the principle of electrocoalescence. In our context, droplet merging is useful for adding reagents to the input samples and combining multiple input samples for pooling. As shown in Fig. 2c, by transporting the droplets to an electrode pair and applying a relatively low voltage (approximately 0.3–1.5 V, depending on the surrounding oil–surfactant composition; Supplementary Note 3 and Supplementary Fig. 7), droplet merging in less than a few seconds can be achieved.

We found that robust and repeatable ferrobotic droplet actuation can be achieved for droplets spanning different ionic strengths and chemical compositions relevant for biological and chemical assays (Extended Data Fig. 3). A total of more than 8 million actuation events were performed over more than 24 h (only limited by the observation time), showing repeatable behaviour over the time period. This behaviour differs from common digital microfluidics approaches such as electrowetting on dielectric, which undergo surface degradation-related issues[30–32]. Further illustrating that other ferrobotic operations are robust, we performed cyclic aliquoting, merging and intermediate transportation of a parent droplet over 800 cycles with less than 1% variation in the corresponding size of the parent droplet post-aliquoting and post-merging (Fig. 2d).

To realize mixing, which is particularly important for homogenizing the droplet contents post-merging, the ferrobot can be oscillated to induce chaotic fluid motion within the merged droplet by alternatively activating the neighbouring coils. As shown in Fig. 2e, the droplet homogenization rate increases with oscillation frequency and, in particular, a nearly full-mixed state can be reached in approximately 15 s by oscillating the ferrobot at 5 Hz.

We used on-board resistive heaters for nucleic acid amplification and sample preparation (for example, lysis). The local temperature can be controlled by adjusting the direct current flowing through the resistive heater, in accordance with the operational needs (Fig. 2f and Extended Data Fig. 4a–c).

We implemented a colorimetric RT-LAMP assay that is based on thermal lysis or inactivation[21] and isothermal amplification (both achievable with on-board resistive heaters). This assay provides a high degree of test accessibility, outweighing the marginal compromise in test accuracy[19,20]. Figure 2g illustrates the RT-LAMP reactions, which involve reverse transcription of the viral RNA, amplification of the product DNA and generation of hydrogen ions, which are colorimetrically detected. By analysing the reaction product (DNA) via gel electrophoresis (Fig. 2h and Supplementary Fig. 1), we verified the assay function in converting and amplifying a SARS-CoV-2-positive control RNA sample. Colorimetric detection is based on the generated hydrogen ions, causing a colour change of an incorporated pH indicator (phenol red) from red-orange to yellow (optimization experiment results are shown in Extended Data Fig. 5a–c). The colour change allows for the binary interpretation of the test, above or below a threshold as positive or negative, respectively. This colour change can be tracked visually (Fig. 2i) by the naked eye, or electronically by integrating an optical sensor (Fig. 2j and Extended Data Fig. 4b,d), without the absorbance of the ferrofluid affecting the readout interpretations. Accordingly, the same limit of detection of 25 cp μl^{-1} of the adopted assay[33] can be achieved in the ferro-droplet format (1 μl; reagent volume of 19 μl; similar to the original assay protocol), which suggests that the magnetic nanoparticles do not interfere with the amplification chemistry or colorimetric readout accuracy (Extended Data Fig. 5d). The assay was also successfully performed by using microfluidic structures of reduced height (approximately 150 μm) to aliquot a tenfold-smaller ferro-droplet volume (100 nl; reagent volume of 1.9 μl; Extended Data Fig. 5e), which is below the volume that can be accurately pipetted using robotic liquid handlers, but useful for minimizing reagent use. Our characterization results also verified the reliability of the assay in the presence of temperature variations of a few degrees Celsius (Supplementary Fig. 2a) and in the presence of biological interferents (Supplementary Fig. 3).

The programmability of our program (Supplementary Fig. 4) allows for its ease of adaptation to streamline the ferrobotic actuation and bioanalytical operations, and deliver versatile RT-LAMP-based testing workflows in an entirely automated manner and with high fidelity.

Illustrating this point in the context of individual sample testing, we customized a disposable microfluidic module to host the input sample, associated reagents and dedicated aliquoting or merging components (Fig. 3a and Extended Data Fig. 4b)—then, augmented it with a PCB module, containing the navigation coils, resistive heater elements and colorimetric sensing circuitry. By programming the PCB at the software level, we installed a ferrobotic instruction set to seamlessly execute the assay. The instruction set charts the navigation plan of a dedicated ferrobot and details the electrode excitation conditions for merging and heating, while accounting for a 5-min heat lysis and a 30-min RT-LAMP reaction period (Fig. 3b).

In this testing workflow, the active ferrobotic operations take place over a period of 1.75 min (Fig. 3c and Supplementary Video 1). A ferro-droplet is first magnetically transported to, then merged and mixed with, an introduced sample droplet to make the sample amenable for ferrobotic manipulation. The next steps in the sequence are aliquoting the ferro-sample, disposing the ferro-sample residue and delivering the aliquot (1 μl) to the reaction chamber (containing the assay reagents). Upon delivery to the reaction chamber, the RT-LAMP process initiates, and after 30 min, the assay readout is colorimetrically quantified, rendering the test result in a sample-to-answer manner. A similar workflow was implemented using microfluidic chips with reduced height to achieve smaller ferro-droplets (approximately 100 nl) for analysis with reduced reagents (Extended Data Fig. 2b).

We assessed the accuracy of our platform with real-world samples by testing 100 clinical samples with the ferrobotic RT-LAMP chip
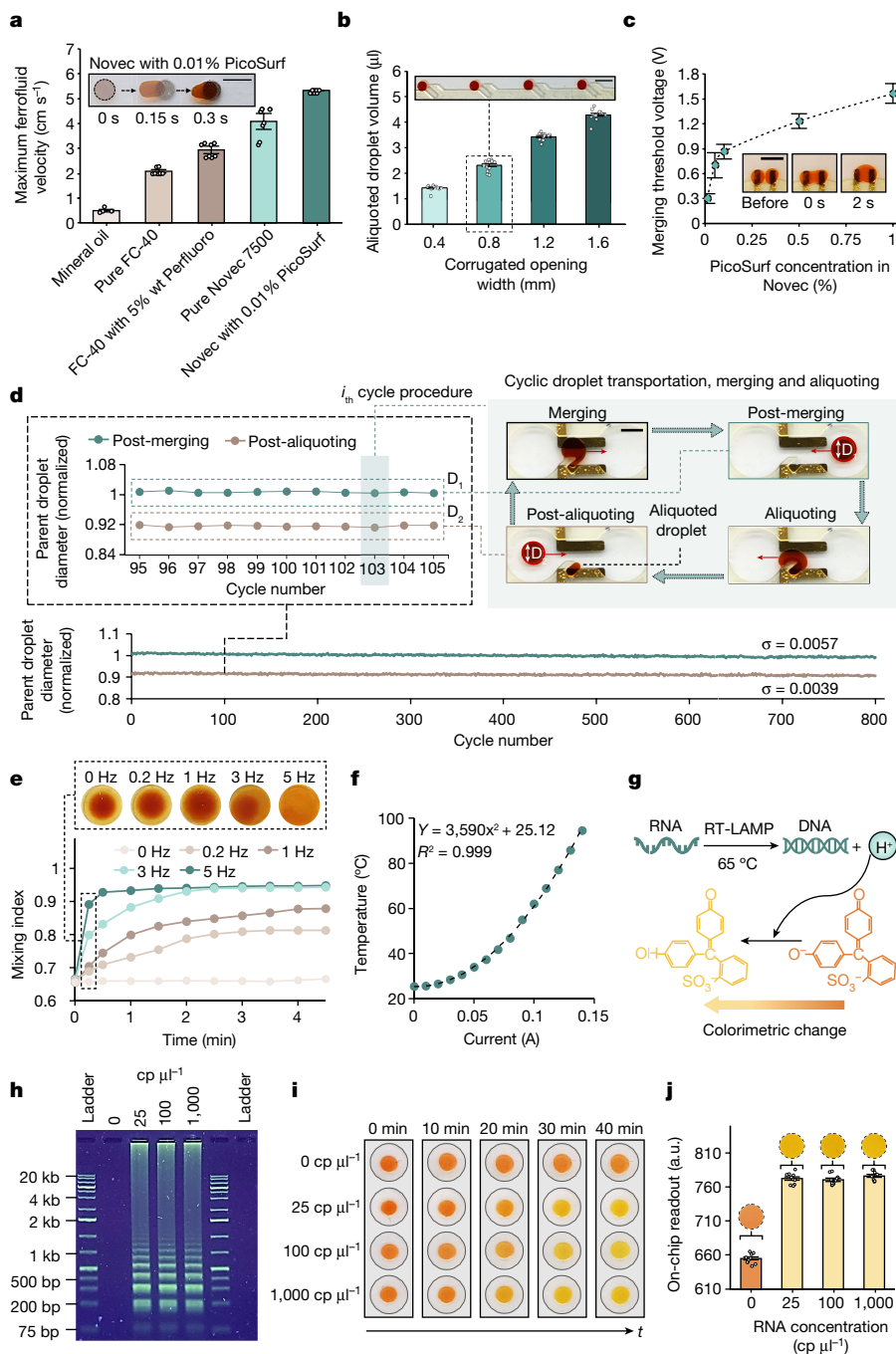
Fig. 2 | Ferrobotic operations enable NAAT-based testing. a, Characterization of the maximum ferro-droplet transportation velocity within different oil environments. The inset shows overlaid sequential images, visualizing the transportation process (scale bar, 3 mm). Error bars indicate mean ± s.e. ($n = 4$ independent experiments). **b**, Characterization of the aliquoted droplet size for different corrugated opening widths (channel height of approximately 900 µm). The inset shows that multiple aliquots of the same ferro-droplet source can be produced by extending the corrugated feature in an array format (scale bar, 5 mm). Error bars indicate mean ± s.e. ($n = 12$ across 3 replicates). **c**, Characterization of the threshold voltage for droplet merging using different concentrations of a surfactant (PicoSurf) within an oil (Novec) environment. The inset shows sequential optical images of the merging process (scale bar, 5 mm). Error bars indicate mean ± s.e. ($n = 3$ independent experiments). **d**, Characterization of the cyclic ferrobotic operations, involving aliquoting, merging and intermediate transportation of a parent droplet to evaluate the robustness of the ferrobotic operations (performed for more than 800 cycles; scale bar, 3 mm). Parent droplet size varied by less than 1% for each of the post-merging and post-aliquoting states (characterized optically). **e**, Progressive mixing index for different actuation frequencies. Corresponding images of the merged droplets under mixing at different actuation frequencies for 15 s are also shown (top). **f**, Characterization of the local temperature set by an on-board resistive heater for different input current. **g**, The RT-LAMP reaction and detection mechanism. **h**, Representative gel electrophoresis analysis of the RT-LAMP reaction product (repeated three times; reaction period of 30 min). **i,j**, Sequential optical images (**i**) and on-chip readouts (**j**) of the RT-LAMP assay performed in ferro-droplets containing negative control and spiked SARS-CoV-2-positive control RNA (25, 100 and 1,000 cp µl^{-1}) samples. Error bars indicate mean ± s.e. ($n = 10$ independent optical sensor readouts).

and comparing the on-chip readouts with the corresponding readouts obtained from the standard PCR with reverse transcription (RT–PCR) and RT-LAMP assays (summarized in Fig. 3d and detailed

in Supplementary Table 6). The collected samples were based on nasopharyngeal swabs from patients infected or uninfected with SARS-CoV-2. The viral on-chip detection threshold (710 a.u.) was
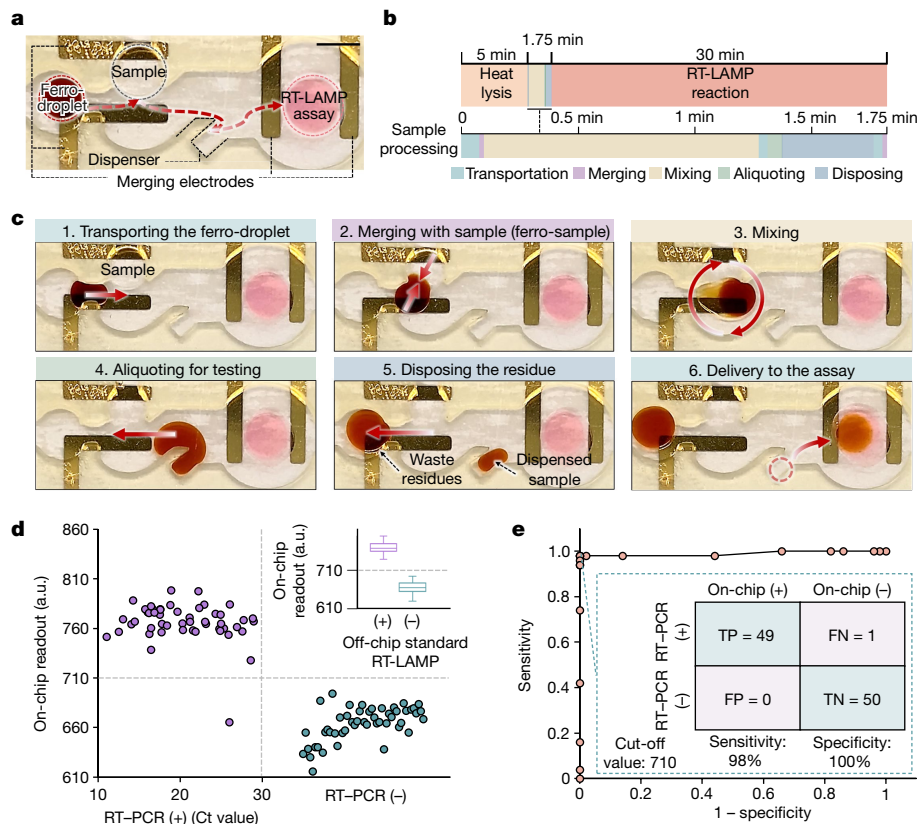
Fig. 3 | Performance of an automated ferrobotic SARS-CoV-2 RT-LAMP workflow for individual clinical sample testing. a, The microfluidic chip for individual sample testing (scale bar, 5 mm). **b**, The timeline of the streamlined on-chip operations for automated individual testing, which includes active ferrobotic sample processing operations over a time window of 1.75 min. Heat lysis and the RT-LAMP reaction were performed at 95 °C and 65 °C, respectively. **c**, Sequential optical images of the active ferrobotic sample processing operations (performed automatically). **d**, Comparison of the ferrobotic SARS-CoV-2 RT-LAMP assay readouts with the corresponding RT–PCR results (Ct values)

for a collection of 100 clinical samples. Each datapoint represents one sample. The inset compares ferrobotically produced versus manually performed RT-LAMP assay results, illustrating that the corresponding sample test results are in complete agreement (whisker limits show extremums, box limits show quartiles and the horizontal line is the median, for the same collection of $n = 100$ samples). **e**, Corresponding receiver operating characteristic curve of the analysed samples. The sensitivity and specificity are based on the set cut-off value of 710 a.u. (also serving as the on-chip detection threshold). FN, false negative; FP, false positive; TN, true negative; TP, true positive.

derived from receiver operating characteristic analysis (aliquoted sample volume of 1 µl).

For all 100 samples, the ferrobotically produced results were in agreement with the manually performed (off-chip) RT-LAMP assay results (100% concordance), illustrating the high fidelity of the ferrobotic automation. Comparison of the ferrobotically produced RT-LAMP-based results with the corresponding results obtained from the RT–PCR assay (gold standard) resulted in a test sensitivity of 98% and specificity of 100% (Fig. 3e), in which the discrepancy in the rare test result can be attributed to the inherent differences of the amplification approaches used[33]. We further validated that the clinical samples with aliquoted volumes of 1 µl and 100 nl can be accurately analysed in a reproducible manner across replicates (Extended Data Fig. 6).

We next demonstrated multiplexed viral testing by utilizing the adaptability of our platform (Extended Data Fig. 7, Supplementary Video 2 and Supplementary Note 4). This testing mode is diagnostically useful for differentiating between the emergent outbreak virus (for example, SARS-CoV-2) and endemic viruses (for example, the seasonal viruses such as influenza A–H1N1) that often result in similar clinical symptoms[34–37].

By utilizing the scalability of the platform, we can increase the testing throughput. The extensibility of the mobile robotic scheme used to a multi-agent mobile (swarm) robotic scheme, together with the expandability of the navigation floor or microfluidic architecture, inherently render our platform scalable. One approach to increasing the throughput is to simply extend our individual testing platform

into an array format (Extended Data Fig. 4a,e). With this implementation, a large number of input samples can be analysed in parallel and asynchronously as they arrive—without involving accumulation wait time (unlike the case for current high-throughput methods that rely on batch processing[38]). A less trivial yet more efficient high-throughput testing approach involves applying our platform to the problem of adaptive pooled testing.

To determine the appropriate number of input samples and guide the pooled testing workflow, we utilized our prevalence-based adaptive testing algorithm that can be implemented following a square matrix pooling scheme. Following this approach, testing efficiency can be substantially improved in moderate-to-low viral prevalence ranges (specifically, by appropriately performing 3^2 or 4^2 matrix pooling, determined algorithmically; Supplementary Note 1).

Figure 4a provides an overview of the algorithm-guided square matrix pooling scheme, particularly for the case of 4^2 pooling, which involves a group of 16 samples arranged in a 4×4 matrix (S_{ij}; i, j represent the row and column indices, respectively). In this scheme, all of the samples are first pooled together and the resultant sample aggregate is analysed by a single assay 'A'. If the assay readout is negative, all of the original input samples will be deemed negative. Otherwise, a second round of testing will be followed. In this round, the samples will be pooled along rows and columns, leading to a total of eight sample aggregates. The row-pooled and column-pooled sample aggregates will be correspondingly analysed by dedicated 'R_i' and 'C_j' assays.
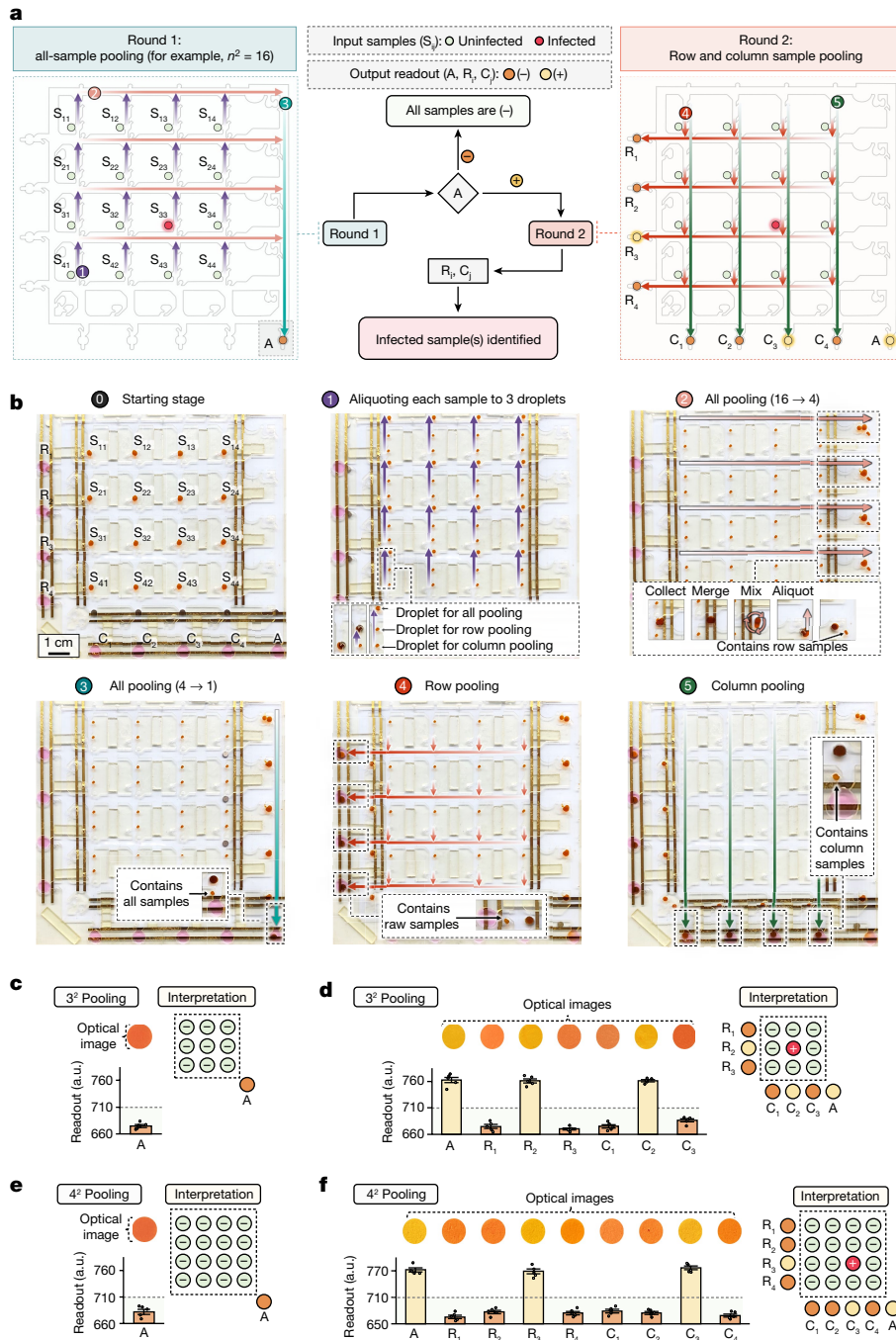
Fig. 4 | Performing a pooled SARS-CoV-2 RT-LAMP workflow using a ferrobot swarm. a, Schematic of the square matrix pooling scheme. The flow chart at the centre provides an overview of the infected sample identification process based on the assay pooled (A) or row–column (R_i/C_j) responses. **b**, Sequential optical images of an automated 4^2 pooling workflow performed by a team of nine ferrobots. To combine aliquots in each pooling step, they were ferrobotically collected, merged, mixed and then dispensed as a 1-μl droplet. The inset images show the critical intermediary ferrobotic operations. **c,d**, Optical images and readouts obtained from ferrobotic pooled testing of two groups of nine clinical samples using the 3^2 pooling chip. The negative assay A response indicated that no infected sample was present among the first group of samples in **c**.

The positive assay A response along with the positive assay R_2 and C_2 responses led to the identification of the infected sample (located at the second row–second column) among the second group of samples (**d**). **e,f**, Optical images and readouts obtained from ferrobotic pooled testing of two groups of 16 clinical samples using the 4^2 pooling chip. The negative assay A response indicated that no infected sample was present among the first group of samples in **e**. The positive assay A response along with the positive assay R_3 and C_3 responses led to the identification of the infected sample (located at the third row–third column) among the second group of samples (**f**). In **c–f**, error bars indicate different trials of optical reading, mean ± s.e. ($n = 5$). Horizontal dashed line indicates on-chip detection threshold (710 a.u.).

The intersectional analysis of the R_i and C_j assay readouts allows for determining the infected sample (or samples) (Fig. 1d and Supplementary Fig. 5). In the relatively low probable cases (for example, 2.5%, assuming a viral prevalence of 2%) in which the paired row–column projections are not one-to-one mapped to specific arrangements of multiple positive samples, only those samples that are deemed suspicious (that is, those located at the intersection of positive row–column projections) will be individually tested.

To implement the square matrix pooled testing workflow, we expanded the microfluidic chip layout for pooled testing. Extended

Article

Data Figure 8a,b illustrates the corresponding layouts of the 3^2 and 4^2 microfluidic chips. The expanded layouts especially include arrays of sample aliquoting interfaces and reaction chambers (containing SARS-CoV-2 RT-LAMP assay solutions), orthogonal corridors for intra-chip sample aliquot transport and extended merging interfaces. To direct the swarm ferrobotic operations in accordance with the devised pooling scheme, we utilized a PCB module with increased navigation coils (that is, an expanded navigation floor) and programmed the PCB module to install an updated multiferrobot-based and pooling algorithm-driven instruction set.

Figure 4b and Supplementary Video 3 illustrate the sequence of the operations performed by a swarm of nine ferrobots to deliver a representative 4^2 pooled testing workflow. The demonstrated sequence involves: (1) making three aliquots of each input sample with the aid of four ferrobots; (2) all-sample pooling to facilitate the first round of testing (performed in two steps; combining the aliquots on the same row using four ferrobots in parallel, followed by combining the resultant aggregates using a single ferrobot); and (3) row–column pooling to facilitate the second round of testing (each performed by a set of four ferrobots). To combine the intended aliquots in each of the pooling steps, the aliquots were ferrobotically collected, merged, mixed and then dispensed as a droplet with a metered volume (1 μl). The overview of the navigation plan and the detailed timeline of the task sequence executed by each ferrobot (in coordination with the other ferrobots) are shown in Extended Data Fig. 8c–f.

Before applying the scaled platform for pooled testing of clinical samples, we evaluated the dilutive effect of sample pooling on the assay detection capability (using positive nasal swab samples). The results indicated the capability of the assay in correctly identifying positive samples with a relatively low viral load, even at dilutions as high as 16 times (Extended Data Fig. 9).

We examined the pooled testing capability of the scaled platform by analysing a collection of 50 clinical samples (pre-characterized via RT–PCR). These samples were grouped in two arrangements of 9 and 16 samples and tested with the corresponding 3^2 and 4^2 chips in a way to allow for evaluating the pooling, detection and interpretation capabilities of the platform in the first and second rounds of testing. Specifically, for each group size or chip, we tested the scenarios that involved the absence or the presence of an infected sample. Figure 4c–f illustrates the corresponding on-chip optical characterization results (with assay reagent volumes of 19 μl to analyse aliquoted samples with volumes of 1 μl). Following the aforementioned testing scheme, by comparing the corresponding assay responses (all-pooled (A) or row–column-pooled (R_i/C_j)) with respect to their detection threshold, we determined the status of each sample. We performed similar pooled testing studies using smaller aliquoted samples (100 nl, with assay reagent volumes of 1.9 μl), demonstrating the ability to reduce reagents further (Extended Data Fig. 10). For all tested scenarios and across all samples, the ferrobotically produced and/or interpreted results were in line with those obtained by RT–PCR.

The demonstrated pooled-testing application, and scale of microfluidic liquid handling operations, is unprecedented. Supplementary Table 1 provides a detailed account of the number of droplet actuation and ferrobotic operations that were reliably carried out to achieve pooled testing. This was achieved by harnessing the competitive advantages of the ferrobotic technology that overcomes performance limits (in terms of reliability, scalability, reagent use and portability, among others) and cost barriers of alternative microfluidics approaches (Supplementary Note 5).

Depending on the situational needs, the ferrobotic testing platform can be adapted—with minimal reconfiguration—to automate other NAAT-based assays (for example, RT–PCR) as well as other pooling schemes (for example, Dorfman[39]). The ferrobotic testing platform can be constructed with low-cost consumables (Supplementary Table 2) and instrumentation (Supplementary Table 3) using widely available materials and circuit components and following existing scalable manufacturing solutions—together enabling mass production for rapid large-scale deployment. As summarized in Supplementary Table 4, we estimate that translating this platform for population-level screening can ultimately lead to approximately three orders of magnitude of increase in marginal gain in testing capacity from the instrumentation investment standpoint, and a 60–300-fold reduction in reagent costs at moderate-to-low viral prevalence (approximately 8% to 0.8%) and tenfold reduction at high viral prevalence. Accordingly, utilizing its high level of accessibility, adaptability and automation, the presented technology can be deployed as a democratized, distributed and decentralized solution to expand our testing capacity for pandemic preparedness. Beyond viral testing, the presented swarm ferrobotic technology can be adapted and scaled to efficiently streamline and massively parallelize various other laboratory-based bioanalytical operations within a miniaturized footprint (Supplementary Note 6). Thus, this technology can serve as a powerful tool for a wide range of biomedical and biotechnological applications such as diagnostics, omics, drug development and chemical and/or biomaterial synthesis.

Online content

Any methods, additional references, Nature Research reporting summaries, source data, extended data, supplementary information, acknowledgements, peer review information; details of author contributions and competing interests; and statements of data and code availability are available at https://doi.org/10.1038/s41586-022-05408-3.

1. Zhu, H. et al. The vision of point-of-care PCR tests for the COVID-19 pandemic and beyond. *Trends Analyt. Chem.* **130**, 115984 (2020).
2. Zhuang, J., Yin, J., Lv, S., Wang, B. & Mu, Y. Advanced 'lab-on-a-chip' to detect viruses—current challenges and future perspectives. *Biosens. Bioelectron.* **163**, 112291 (2020).
3. Sands, P., Mundaca-Shah, C. & Dzau, V. J. The neglected dimension of global security—a framework for countering infectious-disease crises. *N. Engl. J. Med.* **374**, 1281–1287 (2016).
4. Weissleder, R., Lee, H., Ko, J. & Pittet, M. J. COVID-19 diagnostics in context. *Sci. Transl. Med.* **12**, eabc1931 (2020).
5. Mercer, T. R. & Salit, M. Testing at scale during the COVID-19 pandemic. *Nat. Rev. Genet.* **22**, 415–426 (2021).
6. Patchsung, M. et al. Clinical validation of a Cas13-based assay for the detection of SARS-CoV-2 RNA. *Nat. Biomed. Eng.* **4**, 1140–1149 (2020).
7. Vandenberg, O. et al. Considerations for diagnostic COVID-19 tests. *Nat. Rev. Microbiol.* **19**, 171–183 (2021).
8. Cheong, J. et al. Fast detection of SARS-CoV-2 RNA via the integration of plasmonic thermocycling and fluorescence detection in a portable device. *Nat. Biomed. Eng.* **4**, 1159–1167 (2020).
9. Ramachandran, A. et al. Electric field-driven microfluidics for rapid CRISPR-based diagnostics and its application to detection of SARS-CoV-2. *Proc. Natl Acad. Sci. USA* **117**, 29518–29525 (2020).
10. Simpson, S., Kaufmann, M. C., Glozman, V. & Chakrabarti, A. Disease X: accelerating the development of medical countermeasures for the next pandemic. *Lancet Infect. Dis.* **20**, e108–e115 (2020).
11. Mardian, Y., Kosasih, H., Karyana, M., Neal, A. & Lau, C.-Y. Review of current COVID-19 diagnostics and opportunities for further development. *Front. Med.* **8**, 615099 (2021).
12. Valera, E. et al. COVID-19 point-of-care diagnostics: present and future. *ACS Nano* **15**, 7899–7906 (2021).
13. Zhu, H., Fohlerová, Z., Pekárek, J., Basova, E. & Neužil, P. Recent advances in lab-on-a-chip technologies for viral diagnosis. *Biosens. Bioelectron.* **153**, 112041 (2020).
14. Asghari, A. et al. Fast, accurate, point-of-care COVID-19 pandemic diagnosis enabled through advanced lab-on-chip optical biosensors: opportunities and challenges. *Appl. Phys. Rev.* **8**, 031313 (2021).
15. Mutesa, L. et al. A pooled testing strategy for identifying SARS-CoV-2 at low prevalence. *Nature* **589**, 276–280 (2021).
16. Kevadiya, B. D. et al. Diagnostics for SARS-CoV-2 infections. *Nat. Mater.* **20**, 593–605 (2021).
17. Binnicker, M. J. Challenges and controversies to testing for COVID-19. *J. Clin. Microbiol.* **58**, e01695-20 (2020).
18. Barak, N. et al. Lessons from applied large-scale pooling of 133,816 SARS-CoV-2 RT-PCR tests. *Sci. Transl. Med.* **13**, eabf2823 (2021).
19. Larremore, D. B. et al. Test sensitivity is secondary to frequency and turnaround time for COVID-19 screening. *Sci. Adv.* **7**, eabd5393 (2021).
20. Habli, Z., Saleh, S., Zaraket, H. & Khraiche, M. L. COVID-19 diagnostics: state-of-the-art and challenges for rapid, scalable, and high-accuracy screening. *Front. Bioeng. Biotechnol.* **8**, 605702 (2020).
21. Smyrlaki, I. et al. Massive and rapid COVID-19 testing is feasible by extraction-free SARS-CoV-2 RT-PCR. *Nat. Commun.* **11**, 4812 (2020).
22. Ganguli, A. et al. Rapid isothermal amplification and portable detection system for SARS-CoV-2. *Proc. Natl Acad. Sci. USA* **117**, 22727–22735 (2020).

23. Sun, F. et al. Smartphone-based multiplex 30-minute nucleic acid test of live virus from nasal swab extract. *Lab Chip* **20**, 1621–1627 (2020).

24. Lukas, H., Xu, C., Yu, Y. & Gao, W. Emerging telemedicine tools for remote COVID-19 diagnosis, monitoring, and management. *ACS Nano* **14**, 16180–16193 (2020).

25. IGI Testing Consortium. Blueprint for a pop-up SARS-CoV-2 testing lab. *Nat. Biotech.* **38**, 791–797 (2020).

26. Tymm, C., Zhou, J., Tadimety, A., Burklund, A. & Zhang, J. X. J. Scalable COVID-19 detection enabled by lab-on-chip biosensors. *Cell. Mol. Bioeng.* **13**, 313–329 (2020).

27. Pfefferle, S., Reucher, S., Nörz, D. & Lütgehetmann, M. Evaluation of a quantitative RT-PCR assay for the detection of the emerging coronavirus SARS-CoV-2 using a high throughput system. *Euro Surveill.* **25**, 2000152 (2020).

28. Karp, D. G. et al. Sensitive and specific detection of SARS-CoV-2 antibodies using a high-throughput, fully automated liquid-handling robotic system. *SLAS Technol.* **25**, 545–552 (2020).

29. Singh, L. et al. Implementation of an efficient SARS-CoV-2 specimen pooling strategy for high throughput diagnostic testing. *Sci. Rep.* **11**, 17793 (2021).

30. Zhang, Y. & Nguyen, N.-T. Magnetic digital microfluidics—a review. *Lab Chip* **17**, 994–1008 (2017).

31. Mibus, M. & Zangari, G. Performance and reliability of electrowetting-on-dielectric (EWOD) systems based on tantalum oxide. *ACS Appl. Mater. Interfaces* **9**, 42278–42286 (2017).

32. Yu, W. et al. A ferrobotic system for automated microfluidic logistics. *Sci. Robot.* **5**, eaba4411 (2020).

33. Dao Thi, V. L. et al. A colorimetric RT-LAMP assay and LAMP-sequencing for detecting SARS-CoV-2 RNA in clinical samples. *Sci. Transl. Med.* **12**, eabc7075 (2020).

34. Ji, M. et al. Automated multiplex nucleic acid tests for rapid detection of SARS-CoV-2, influenza A and B infection with direct reverse-transcription quantitative PCR (dirRT-qPCR) assay in a centrifugal microfluidic platform. *RSC Adv.* **10**, 34088–34098 (2020).

35. Yu, L. et al. Simultaneous detection of SARS-CoV-2 and pandemic (H1N1) 2009 virus with real-time isothermal platform. *Heliyon* **7**, e07584 (2021).

36. Mancini, F. et al. Multiplex real-time reverse-transcription polymerase chain reaction assays for diagnostic testing of severe acute respiratory syndrome coronavirus 2 and seasonal influenza viruses: a challenge of the phase 3 pandemic setting. *J. Infect. Dis.* **223**, 765–774 (2021).

37. Stambaugh, A. et al. Optofluidic multiplex detection of single SARS-CoV-2 and influenza A antigens using a novel bright fluorescent probe assay. *Proc. Natl Acad. Sci. USA* **118**, e2103480118 (2021).

38. Peeling, R. W., Olliaro, P. L., Boeras, D. I. & Fongwen, N. Scaling up COVID-19 rapid antigen tests: promises and challenges. *Lancet Infect. Dis.* **21**, e290–e295 (2021).

39. Dorfman, R. The detection of defective members of large populations. *Ann. Math. Stat.* **14**, 436–440 (1943).

Article

Methods

Materials and reagents for ferrobotic platform and viral testing

The ferrofluid used in this work is ferumoxytol, a US Food and Drug Administration-approved intravenous iron preparation (AMAG Pharmaceuticals). Rare earth permanent magnets (D101 and DH2H2, with corresponding thickness of 0.8 mm and 5 mm, and diameter of 2.54 mm and 5 mm) were purchased from K&J Magnetics for device construction and characterization. The microfluidic module was constructed from double-sided tape (3M, 300LSE) and transparent polyethylene terephthalate (PET) film layers (M.G. Chemicals). The microfluidic devices were filled with Novec 7500 Engineered oil (3M) containing 0–0.1% surfactant (PicoSurf 1; Sphere Fluidics), unless stated otherwise. Other oils including mineral oil (Sigma-Aldrich), FC-40 and corresponding surfactant ($1H,1H,2H,2H$-perfluoro-1-decanol; Sigma-Aldrich) were also used for velocity characterization. Single-stranded RNA fragments of SARS-CoV-2 (10^8 copies per microlitre) were purchased from Sigma-Aldrich. Living *Escherichia coli* K-12 strain (3×10^5 colony-forming units (c.f.u.) μl^{-1}) in liquid nutrient broth was purchased from Carolina Biological Supply. A SARS-CoV-2 Rapid Colorimetric RT-LAMP Assay Kit was purchased from New England Biolabs and stored at −20 °C. The viral transport media were purchased from BD. The UCLA Clinical Microbiology Laboratory performed RT–PCR using the following assay: TaqMan COVID-19 RT–PCR Assay (Thermo Fisher Scientific).

Electromagnetic navigation floor circuit design

To manipulate ferrobots across 2D space, an electromagnetic (EM) navigation floor on PCB comprised active coil elements in a 2D-array format. Each element had a three-turn coil with a size of 1.5 mm × 1.5 mm traced onto the three layers of the PCB, with a 0.1-mm gap separated from adjacent elements. Each coil element can be activated by a direct current (DC) of 0.2 A, generating a localized magnetic force that attracts the ferrobot (Supplementary Fig. 8). Programmable current source integrated circuits (ICs) LT3092 (Linear Technology) were used to power the actuated coils (3 V, 0.6 W for each actuated coil). Programmable switch ICs MAX14662 (Maxim Integrated) were used to selectively activate the EM coils and components.

To enable scalable asynchronous parallel testing of 32 samples, the individual testing navigation floor comprised an array of 4 × 8 testing units. Each testing unit included two 20-Ohm resistive heaters, an array of 14 EM coils and an optical sensing module containing a white-light LED (20 mA) and an ambient light sensor (3.3 V) with a 560-nm peak absorbance (BH1721, ROHM Semiconductor). The optical components were operated with stable supply conditions, minimizing signal drift.

Each EM coil element was individually addressed by the output of a switch IC. The matrix-format navigation floor was designed for general ferrobotic operations and testing applications, comprising an active matrix array of EM coil elements, which was specifically selected when switch ICs activate corresponding rows and columns in the navigation floor (Extended Data Fig. 4f). Switch ICs were controlled via serial peripheral interface by an Arduino Nano, which in turn communicated with a computer through serial communication. Target coordinates preprogrammed or sent from the user interface were translated to serial peripheral interface commands by the Arduino and then transmitted to switch ICs for addressable activation of the EM coils. The EM navigation floor can be functionalized with benchtop instruments (laptop and power supplies) or as a self-sufficient battery-operable handheld unit (Supplementary Fig. 9 and Supplementary Video 4).

Microfluidic device fabrication

The microfluidic chips were fabricated by assembling layers of double-sided tape and transparent PET film sheets. In particular, one and six layers of double-sided tape were used to construct microfluidic chips with corresponding heights of approximately 150 μm and 900 μm. Patterns were laser cut into the double-sided tape and PET to make microchannels (VLS 2.30, Universal Laser System). The double-sided tapes and PET sheets were then thoroughly cleaned by immersing them in an acetone ultrasonic bath for 5 min, followed by repeating this cleaning process with isopropyl alcohol and deionized water. To completely dry the cleaned microfluidic layers, the devices were baked at 65 °C for 4 h. To make the surface of the microchannels hydrophobic, the inner surface of double-sided tape and PET sheets were exposed by a shadow mask and treated with NeverWet base-coat spray (Rust-Oleum), followed by resting for 30 min. The devices were then again treated with NeverWet top-coat spray, followed by incubation at room temperature for 12 h. The droplet merging electrodes were patterned on PET sheets by photolithography using positive photoresist (AZ5214E, MicroChemicals), followed by the evaporation of 20 nm of Cr and 100 nm of Au and a lifting-off step in acetone. The fabricated microfluidic devices were preloaded with oils containing various concentrations of surfactants and reagents for experiments.

Maximum transportation velocity characterization within different oil environments

Microfluidic devices with 50 × 30 × 0.7-mm inner chambers were fabricated and assembled. A ferrobot was placed on top of the navigation floor and below the microfluidic device. Microfluidic chambers filled with different oils including mineral oil, FC-40 (with or without 5% Perfluoro) or Novec 7500 (with or without 0.01% PicoSurf) were used for velocity characterization. After the ferrofluid droplets (2 μl) were loaded in the microfluidic chambers, these droplets moved along with the ferrobot, which was sequentially guided by the EM coils actuation in an array from left to right. The velocity of the ferrobot was controlled by adjusting the time interval between activating two adjacent coils. If the ferrofluid droplet followed the ferrobot to the end successfully, then the velocity of the magnet would increase by shortening the actuation time interval (by 1 ms) in the next round until the droplet failed to follow the magnet.

Droplet aliquoting characterization setup and procedure

To validate the aliquoting operation in the optimized oil environment, microfluidic devices (with heights of approximately 150 μm or 900 μm) containing various corrugated wall structures were designed. Devices with different opening widths (0.2, 0.4, 0.8, 1.2 and 1.6 mm) at the corrugated wall were fabricated, assembled and tested. After a parent ferrofluid droplet was loaded in each device (2 μl and 10 μl for devices with channel heights of 150 μm and 900 μm, respectively), it was transported by the ferrobot along the same-sized repeated corrugated structures to aliquot smaller ferro-droplets. The aliquoted droplets were imaged to measure the droplet size.

Merging characterization setup and procedure

A microfluidic device for merging and mixing was fabricated and assembled, with patterned electrocoalescence electrodes (1-mm width, spaced 2 mm apart, thicknesses of 20 nm of Cr and 100 nm of Au) on PET substrate. To characterize merging, after two 5 μl ferrofluid droplets were loaded in each microfluidic device filled by Novec 7500 with different PicoSurf surfactant concentrations (0.01%, 0.05%, 0.1%, 0.5% and 1%), the two droplets were manipulated by the ferrobot to the vicinity of the actuation electrode. A gradually increased (increments of 0.1 V) DC voltage was applied between the two electrodes until the droplets merged.

Mixing characterization setup and procedure

To characterize active mixing, the device was loaded with one 5-μl coloured ferrofluid droplet and one 5-μl transparent water droplet. After merging, the underlying ferrobot was directed to induce chaotic fluid motion within the merged droplet with different frequencies (0.2, 1, 3 and 5 Hz). A video recording was taken for the mixing process, and the droplet homogenization rate was calculated through image processing.

To quantify mixing efficiency, the video frames were imported into MATLAB, and the pixel data (in greyscale) at the droplet region were extracted. A mixing index is defined as:

$$\text{Mixing index} = 1 - \sqrt{\frac{1}{N-1}\sum_{i=1}^{N}\frac{(c_i - c_{\text{ave}})^2}{c_{\text{ave}}^2}}$$

where N, c_i and c_{ave} are the total number of pixels, the greyscale values at pixel i and the average greyscale values over N pixels, respectively.

Characterization of long-term cyclic ferrobotic operations
A microfluidic device that contains two chambers and a connection channel in between was fabricated and assembled. The connection channel contains a corrugated wall structure and a pair of merging electrodes deposited on the PET substrate. After a 7.0-µl ferro-droplet was loaded into the microfluidic chamber, the ferrobot manipulated the ferro-droplet periodically: dispense the droplet into mother and daughter droplets when transporting from the right chamber to the left chamber, and merge the mother droplet with the dispensed droplet when transporting from the left chamber to right chamber. These actions were repeatedly performed for more than 800 cycles. Images were taken during the whole process, and the dynamic variation of the droplet size was measured through image analysis. To demonstrate the extreme reliability of the ferrobotic droplet actuation across different ionic strength and chemical conditions, 10 droplets with differing compositions (H_2O, PBS, 0.1 M and 1 M HCl, 0.1 M and 1 M KCl, 0.1 M and 1 M NaCl, and 0.1 M and 1 M NaOH) were actuated by designated ferrobots over more than 70,000 cycles (12 commuted pixels per cycle per ferrobot) and 24 h. The actuation events and commuted pixels are tracked by monitoring the current through the designated impedance sensing gold electrode pairs (with the aid of CH Instrument 660E; applied voltage of 1 V).

Programmable heating characterization setup and procedure
To implement programmable heating, a microfluidic device was placed on the PCB that contained resistive heaters. The heated region in the chip was placed right above the location of the resistive heater. Copper cubic blocks (3 mm in length, 0.8 mm in width and 2 mm in height) were placed between the PCB surface and the microfluidic chip for heat transduction. To characterize the heating function, different current was applied through the resistive heater (0–0.14 A), inducing a temperature increase by Joule heating. The temperature was then measured by a thermocouple. By programming the current through the resistive heater, the local temperature could be set in relation to the surrounding temperature (Supplementary Fig. 2b,c). If increased precision control of local temperature is desired, a temperature sensor can be integrated to form an internal real-time closed-loop temperature control mechanism.

Off-chip RT-LAMP characterization
To detect RNA, RT-LAMP assays were conducted at room temperature. As the standard protocol described by NEB, every 25-µl RT-LAMP assay included 12.5 µl WarmStart Colorimetric RT-LAMP 2X master mix, 2.5 µl guanidine hydrochloride, 2.5 µl target RNA primer mix, 5.5 µl nuclease-free water and 2 µl input sample. To characterize the RT-LAMP assay for SARS-CoV-2 detection, single-stranded RNA fragments of SARS-CoV-2 diluted to various concentrations (0, 25, 100 and 1,000 copies per microlitre) were mixed with the assay as input sample, then the RT-LAMP assays were incubated at 65 °C for 30 min. After incubation, the assays were further analysed by Nanodrop One (Thermo Fisher Scientific) and gel electrophoresis. Plate reader Cytation 5 (BioTek) was also used to record the assay absorbance (at 560 nm) during incubation (at 65 °C) using a 384-well plate.

RT-LAMP characterization within the ferrobotic chip
To characterize the RT-LAMP assay performance within the ferrobotic chip, a 20-µl RT-LAMP assay containing ferrofluid was prepared for the on-chip reaction. The compositions of the assay were: 10 µl WarmStart Colorimetric RT-LAMP 2X master mix, 2 µl guanidine hydrochloride, 2 µl target RNA primer mix, 5 µl nuclease-free water and 1 µl input sample. The input sample contained single-stranded RNA fragments of SARS-CoV-2 in various concentrations (0, 25, 100 and 1,000 copies per microlitre) and 13% of ferumoxytol. The RT-LAMP assays were loaded in the testing microfluidic device and incubated at 65 °C for 30 min. The incubation process of the assay was recorded by video. After the RT-LAMP reaction, the colour was quantitatively measured by the optical sensing module. A similar procedure was performed with a 2-µl RT-LAMP assay and using microfluidic devices with reduced height (approximately 150 µm), when characterizing the response of the assay to 100 nl input samples.

Standard RT–PCR test for clinical samples
The TaqPath COVID-19 RT–PCR assay targets the SARS-CoV-2 genes encoding S, N and ORF1ab. Extraction was performed on the automated KingFisher Flex Purification System. RT–PCR was performed on the Applied Biosystems 7500 Real-Time PCR Instrument. Detection of two or more targets was considered positive. All testing was performed on nasopharyngeal swabs collected from symptomatic patients. The Ct values were extracted from each instrument and represent a midpoint between the target genes.

Off-chip RT-LAMP detection for clinical samples
All clinical samples were obtained following approval from the University of California, Los Angeles, Institutional Review Board (IRB#21-000982). Clinical samples were collected using a nasal swab, stored in the viral transport media at −80 °C, and added into PBS buffer (20% viral transport media + 80% PBS buffer) with inactivation reagent (including 6 mM NaOH for adjusting pH, 2.5 mM TCEP-HCl and 1 mM EDTA). For the off-chip RT-LAMP test, the samples were placed in a heat block set to 95 °C for 5 min to be inactivated. RT-LAMP assays were prepared following the off-chip protocol and incubated at 65 °C for 30 min. Optical images were taken after the incubation.

Ferrobotic individual clinical sample testing
To perform ferrobotic SARS-CoV-2 individual tests on clinical samples, microfluidic devices containing a sample input chamber, a ferrofluid chamber, an assay chamber, two pairs of merging electrodes (patterned at the sample input chamber and the assay chamber) and a dispensing structure were fabricated and assembled. Each microfluidic chip was preloaded with a ferrofluid droplet (50% ferumoxytol) in the ferrofluid chamber and the RT-LAMP assay solution in the assay chamber (reagent volumes of 1.9 µl and 19 µl for analysis of 100 nl and 1 µl aliquoted samples, respectively). For clinical sample analysis, the starting sample was pipetted into the microfluidic chip at the sample input chamber (via the designated sample inlet). Specifically, 0.52 µl and 5.2 µl of starting samples were correspondingly used for subsequent aliquoting or analysis of 100-nl and 1-µl droplets. Then, heat inactivation and lysis were performed on the PCB for 5 min by powering a 20-Ohm resistive heater with 0.14 A DC current. Thereafter, a ferrobot performed the sample processing steps of transportation, merging, mixing, aliquoting, disposal and delivery to the assay. Then, the on-chip RT-LAMP reaction (at 65 °C) continued for 30 min. The assay readout was measured by the optical sensing module.

Ferrobotic multiplexed testing
For multiplexed detection of SARS-CoV-2, influenza A–H1N1 and rActin RNA, a microfluidic device with a sample input chamber, a ferrofluid chamber, an assay chamber array, two pairs of merging electrodes (patterned at the sample input chamber and across the assay chamber array) and a dispenser array was fabricated and assembled. Each microfluidic chip was preloaded with a ferrofluid droplet in the ferrofluid chamber and three 19-µl RT-LAMP reaction solutions, containing primers for

Article

SARS-CoV-2, influenza A–H1N1 (Thermo Fisher Scientific) and internal control (NEB), respectively, in the assay chamber array. When performing a validation test, a blank sample or negative nasal swab sample either with or without target (spiked with SARS-CoV-2 and/or an influenza A–H1N1-positive control) was loaded into the microfluidic chip at the sample input chamber. Inactivation or lysis was then performed on the PCB for 5 min by powering a 20-Ohm resistive heater with a 0.14 A DC current. Thereafter, a ferrobot performed the sample processing steps of transportation, merging, mixing, aliquoting, disposal and delivery to the assays. Each RT-LAMP assay solution ended up receiving a 1 µl ferro-sample. Then, the on-chip RT-LAMP reaction (at 65 °C) continued for 30 min. The readout for each assay was measured by the optical sensing module.

Ferrobotic pooled clinical sample testing

For pooled tests of clinical samples, microfluidic devices with a matrix array of sample input chambers, dispensers, two arrays of assay chambers and five pairs of merging electrodes (patterned across the assay well arrays and mixing regions) were fabricated and assembled. The assay chambers were preloaded with RT-LAMP assay solutions (reagent volumes of 1.9 µl and 19 µl for 100 nl and 1 µl aliquoted samples, respectively). A number of 3.5-µl heat-inactivated starting ferro-samples were loaded into the input chambers (9 for 3^2 and 16 for 4^2 pooling testing). Thereafter, ferrobots performed the sample processing steps of several rounds of aliquoting, transportation, merging, mixing and delivery to the corresponding assay chambers. The navigation planning of the ferrobots accounted for the maintenance of an inter-ferrobot distance of 10 mm to avoid inter-ferrobot magnetic interference. The on-chip RT-LAMP reaction took place for 30 min (at 65 °C). The assay readout was measured by the optical sensing module.

RT-LAMP validation in a diluted clinical sample

Five nasal swab samples (originally obtained from donors infected with COVID-19, pre-characterized via RT–PCR) with various Ct values (11, 15.7, 21.16, 24.97 and 28.95) were diluted in PBS with different dilution rates (4, 9, 16 and 25). Then, all of the diluted and undiluted samples were tested by both standard off-chip RT-LAMP and on-chip RT-LAMP testing. The reaction products of standard off-chip RT-LAMP were visually recorded in tubes. The reaction products of on-chip individual RT-LAMP were visually recorded in the microfluidic chips, then quantitatively measured by the optical sensing module.

Reporting summary

Further information on research design is available in the Nature Research Reporting Summary linked to this article.

Data availability

All data needed to evaluate the findings and conclusions in the paper are present in the paper and/or Supplementary Information, and can be accessed through the Open Science Framework at https://osf.io/ac9hz/?view_only=7b610238e37848faa05c89b7aa48e54a (https://doi.org/10.17605/OSF.IO/AC9HZ).

a

1. Laser-cut

Laser

Sample inlet

PET

Double-sided tape

PET

2. Superhydrophobic surface treatment

Spray source

3. Vertical assembly

Sample inlet

b

Δt = 0.25 s — Mineral oil

3 mm — Pure FC 40

FC 40 w/ 5% perfluoro

Pure Novec 7500

Novec w/ 0.01% Picosurf

c

Corrugated opening width (mm)

0.4

0.8

1.2

1.6

5 mm

d

Droplet volume (μL)

$y = 0.24x^2$
$R^2 = 0.99$

Droplet diameter (mm)

Extended Data Fig. 1 | Fabrication of microfluidic chips and characterization of ferrobotic operations. a, Fabrication process of the microfluidic chip (*e.g.*, individual testing chip). **b**, Optical images of ferro-droplet-carrying ferrobots at Δ*t* = 0.25 s, visualizing the maximum achievable transportation velocities within different oil environments. In all cases, the ferrobots are programmed to travel at the highest possible velocity that allows for the ferro-droplets to keep up with the underlying ferrobot movement. **c**, Optical images of the arrays of aliquoted droplets for different corrugated opening widths. **d**, Relationship between the ferro-droplet diameter and volume. Insets show optical images of the ferro-droplets.
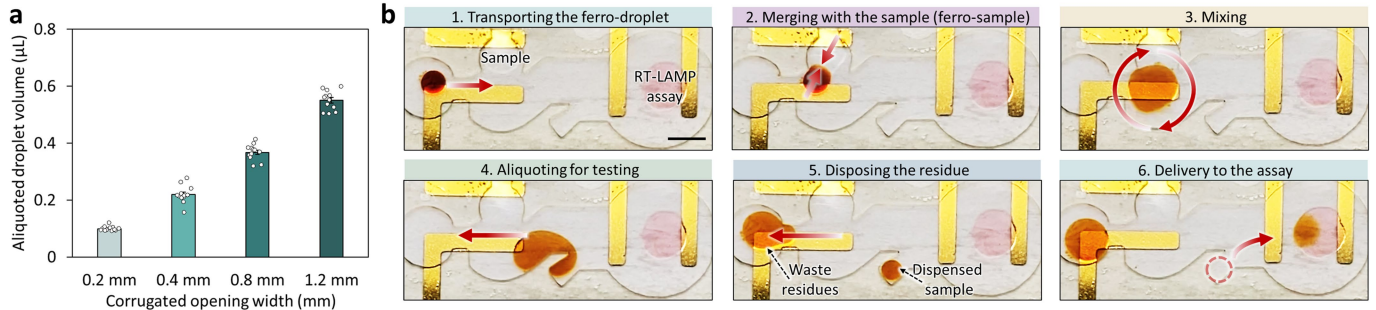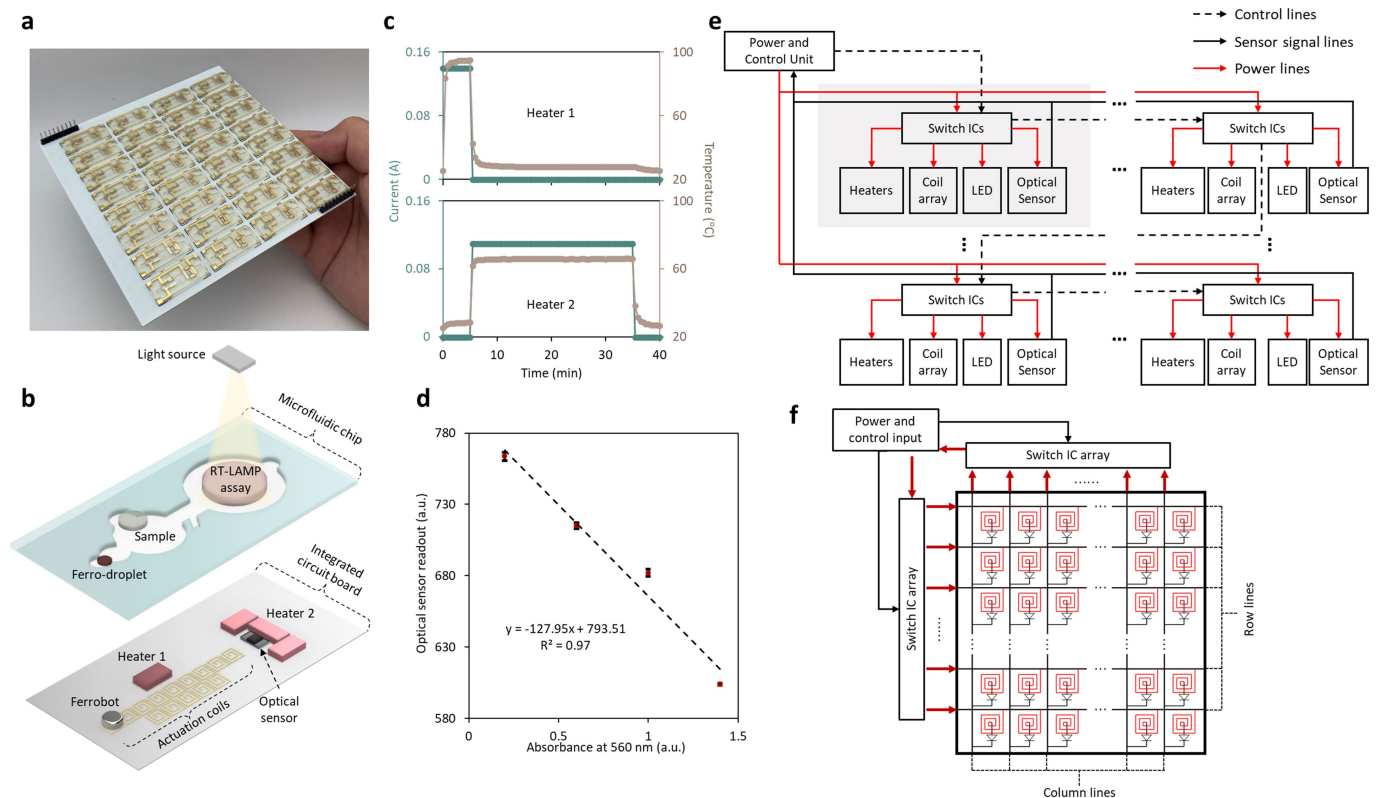
Extended Data Fig. 2 | Characterization and demonstration of ferrobotic operations in small sample volume device. a, Characterization of the aliquoted droplet volume for different corrugated opening widths (channel height: ~150 µm). Error bars, mean values ± SE (n = 12 across 4 replicates). **b**, Sequential images of the active ferrobotic sample processing operations in a small sample volume device (dispensed sample ~ 100 nL; scale bar: 5 mm).
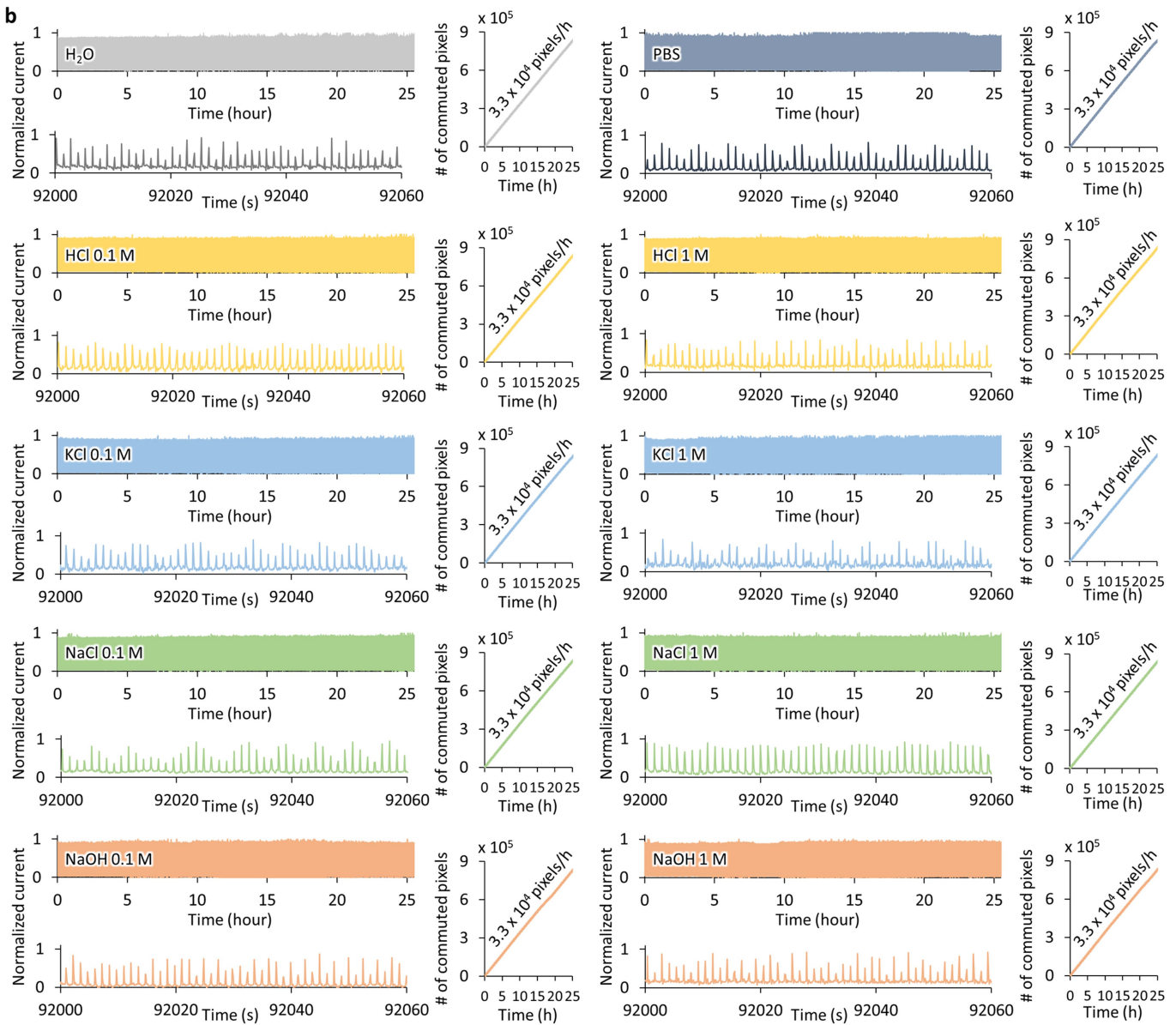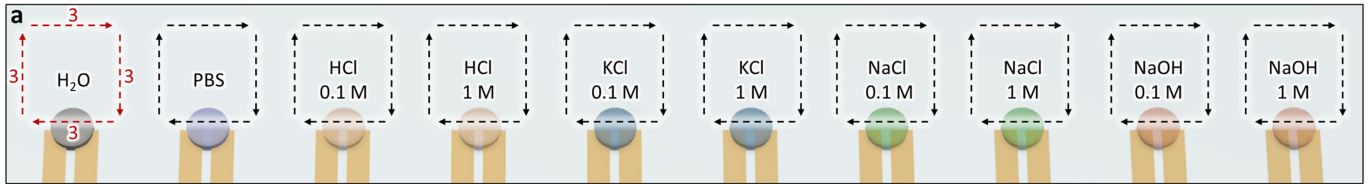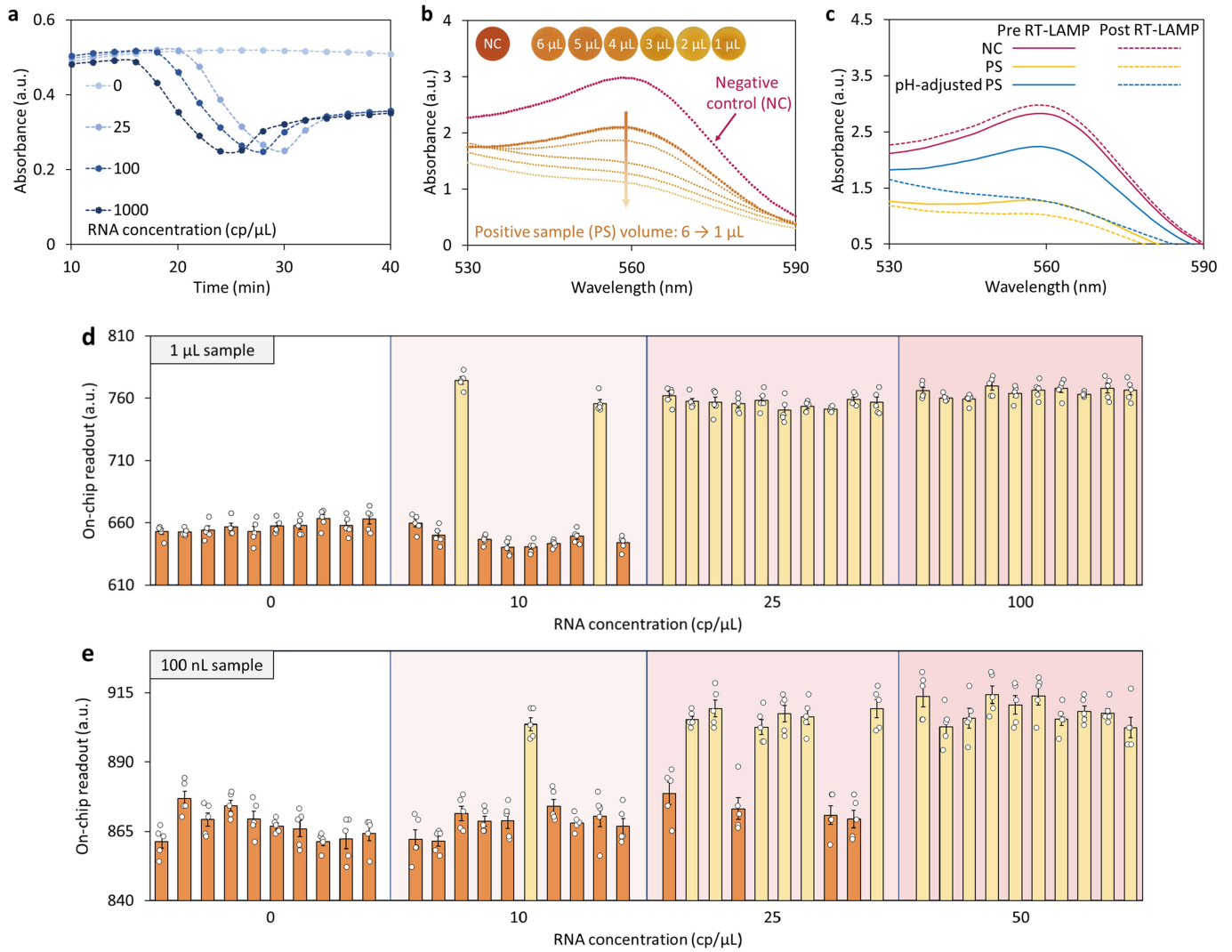
Extended Data Fig. 3 | Characterization of the robustness of ferrobotic actuation over a range of ferro-droplet ionic strengths and chemical conditions. a, Schematic of the characterized ferrobotic actuation, involving cyclic actuation of 10 ferro-droplets (with differing ionic strengths and chemical conditions) by designated ferrobots (12 commuted pixels-per-cycle/ferrobot). The actuation events and commuted pixels are tracked by monitoring the current through impedance sensing electrode pairs. **b**, Corresponding normalized measured current through the electrode pairs and accumulated commuted pixels over time (based on the recorded current peaks) are shown, resulting in a total of > 8 million actuation events over > 24 h (only limited by observation time).

Extended Data Fig. 4 | Demonstration of fully integrated platform and component characterization. a, Optical image of a representative multi-sample ferrobotic platform for individual testing (here, 32 test sites). **b**, Exploded schematic of the microfluidic layer and actuation/sensing layer for a ferrobotic viral testing device designed for individual testing. **c**, Programmed input current profiles of two neighboring (12-mm apart) on-board resistive heaters and the correspondingly established local temperature profiles. **d**, Characterization of optical sensor readout *versus* standard Nanodrop readout (using solutions containing different concentrations of a pink color dye. Error bars, mean values ± SE (n = 5 independent optical sensor readouts). **e**, Schematic diagram of the circuitry for a multi-sample individual testing PCB (extended into an array format). **f**, Schematic diagram of the control circuitry used for multiplexed testing (featuring an expanded coiled navigation floor).

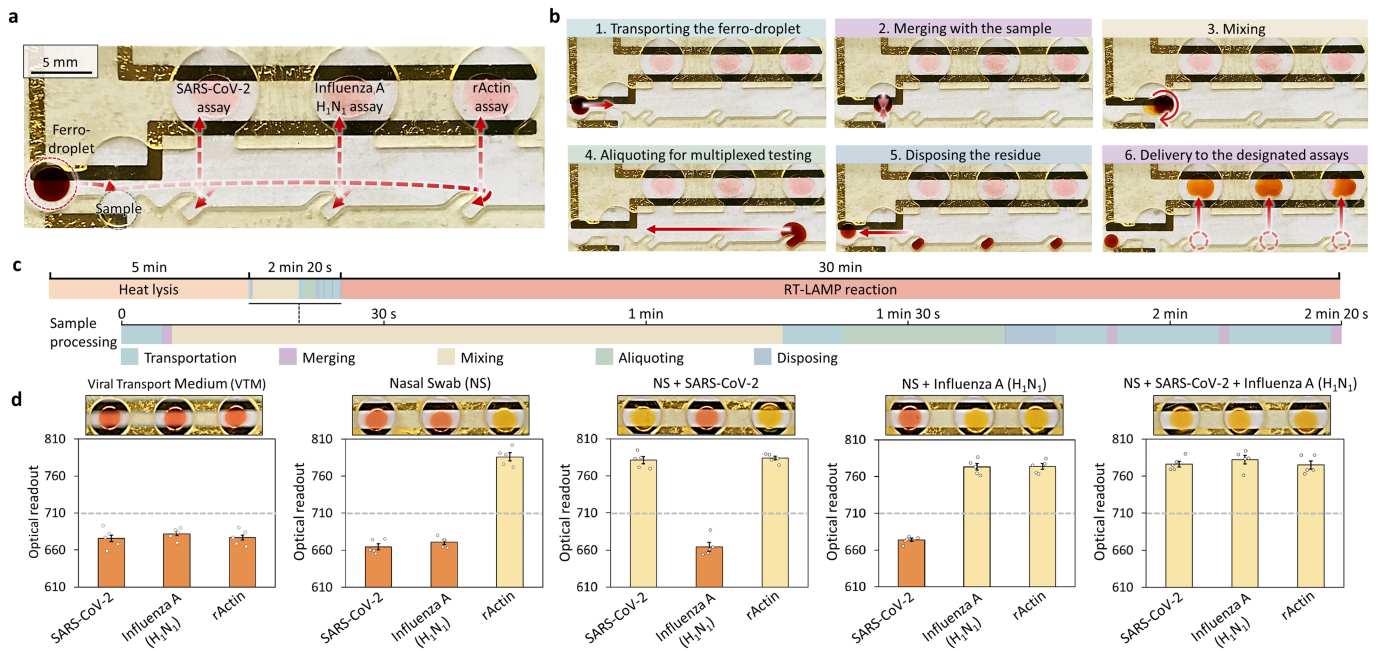**Extended Data Fig. 5 | Characterization of the colorimetric RT-LAMP assay. a**, Quantification of the RT-LAMP assay response by real-time absorbance measurement using a plate reader. **b**, Absorbance spectra and corresponding optical images (insets) of the RT-LAMP reaction products for different volumes of positive input samples (6 to 1 μL, reaction period: 30 min). **c**, Absorbance spectra of the RT-LAMP assay solution pre- and post-RT-LAMP reaction, showing the utility of the assay pH adjustment for optimizing the assay's colorimetric response. **d, e**, RT-LAMP colorimetric readout for ferro-droplet sample volumes of 1 μL **(d)** and 100 nL. **(e)**, across various input SARS-CoV-2 RNA copy numbers or negative controls (10 independent tests per condition). Limits of detection of 25 cp/μl and 50 cp/μl are observed for the 1 μL and 100 nL sample respectively, likely limited by statistical sampling errors when copy number approaches ~1 per sample volume. Error bars, mean values ± SE (n = 5 independent optical sensor readouts).

Article
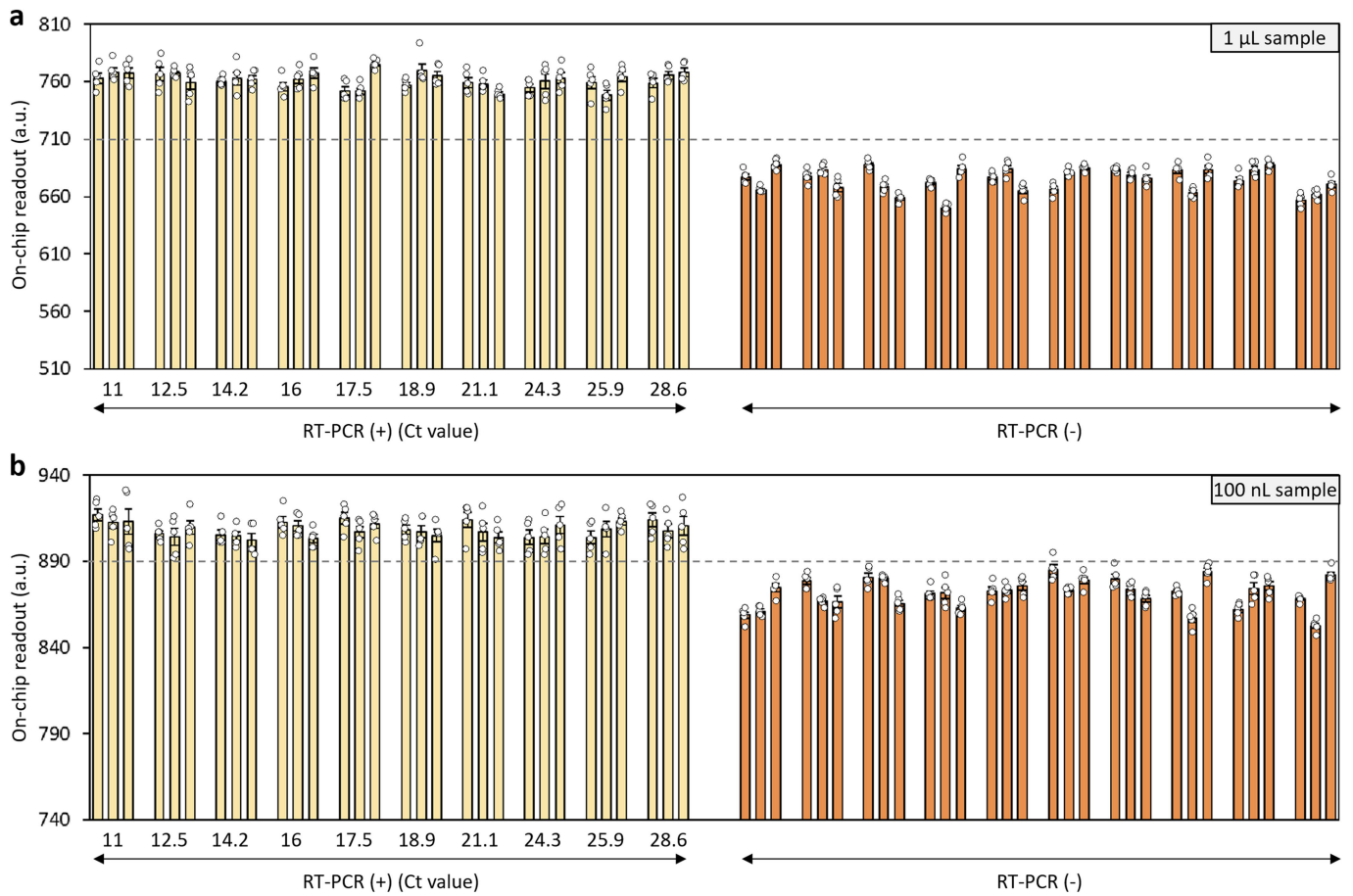
Extended Data Fig. 6 | Repeatability and reproducibility of ferrobotic tests with clinical samples. a, b, Ferrobotic SARS-CoV-2 RT-LAMP assay readouts corresponding to ferro-droplet sample volumes of 1 μL **(a)** and 100 nL **(b)**. Clinical samples from 10 SARS-CoV-2 infected and 10 uninfected patients (pre-characterized via RT-PCR) were analyzed across three replicates for each sample volume. Error bars indicate different repeats of colorimetric reading, mean values ± SE (n = 5). The colorimetric detection threshold for positivity for the 1 μL- and 100 nL-test sample volume cases is correspondingly 710 a.u. and 890 a.u. in our system.

a, **b**,
1. Transporting the ferro-droplet
2. Merging with the sample
3. Mixing
4. Aliquoting for multiplexed testing
5. Disposing the residue
6. Delivery to the designated assays

Extended Data Fig. 7 | Ferrobotically-automated RT-LAMP for multiplexed testing. a, Annotated image of the microfluidic chip for multiplexed testing. **b**, Sequential optical images of the active ferrobotic sample processing operations (performed automatically). **c**, The timeline of the streamlined on-chip operations for automated multiplexed testing, which includes active ferrobotic sample processing operations over a time window of 2:20 min:s.

d, Optical images and corresponding on-chip readouts of the SARS-CoV-2, influenza A–H1N1, and rActin (internal control, IC) RT-LAMP assays for different combinations of input samples (spiked with corresponding RNAs). Nasal Swab (NS) samples naturally contain rActin. Error bars indicate different trials of optical reading, mean values ± SE ($n = 5$).
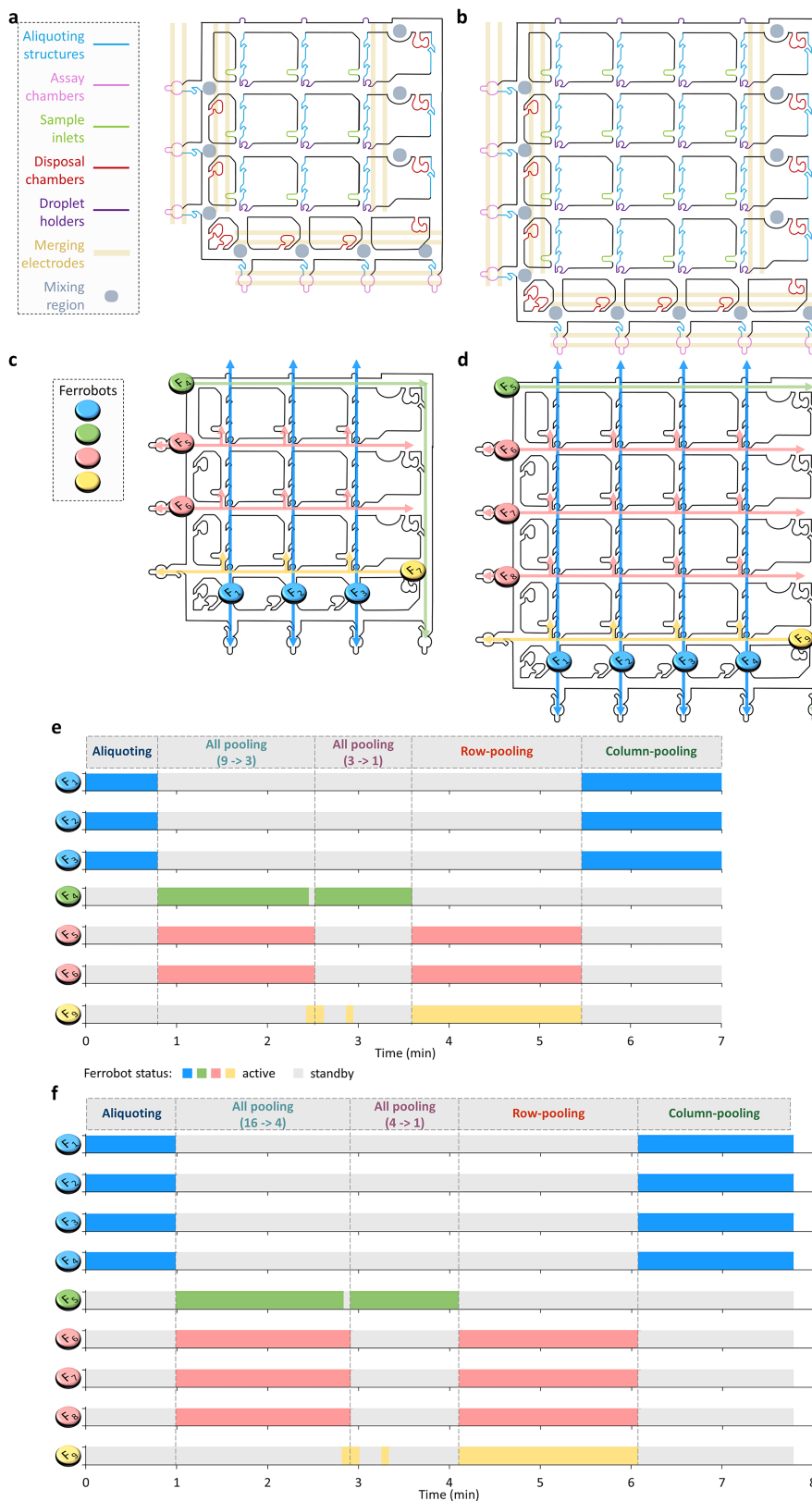
Extended Data Fig. 8 | Microfluidic chip layouts and the ferrobot navigation plans and task assignment for pooled testing. a, **b**, Schematic illustration of the microfluidic chip layout for 3^2 (**a**) and 4^2 (**b**) pooled testing (key features are outlined and labeled). **c**, **d**, Overview of the navigation plans of seven and nine ferrobots for 3^2 (**c**) and 4^2 (**d**) pooled testing. Each F_i represents an individual ferrobot. **e**, **f**, The timeline of the ferrobots' assigned tasks and status (active, standby) for 3^2 (**e**) and 4^2 (**f**) pooled testing.
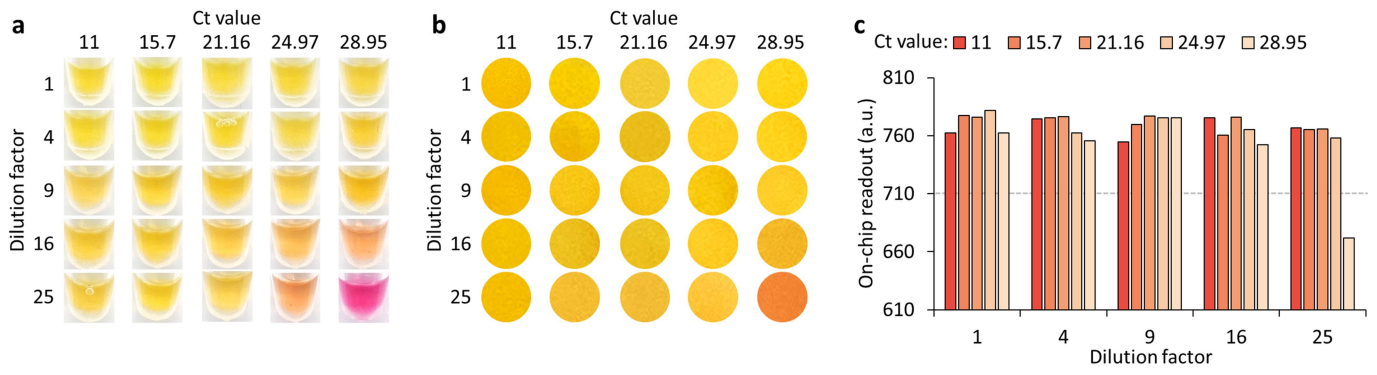
Extended Data Fig. 9 | Detection of virus in diluted and undiluted clinical samples by colorimetric SARS-CoV-2 RT-LAMP assay. a, b, Optical images of the standard assay responses in microfuge tubes (**a**) and on-chip assay responses (**b**) for undiluted or diluted patient samples with different Ct values. **c,** Corresponding optical readouts of the on-chip assay responses.
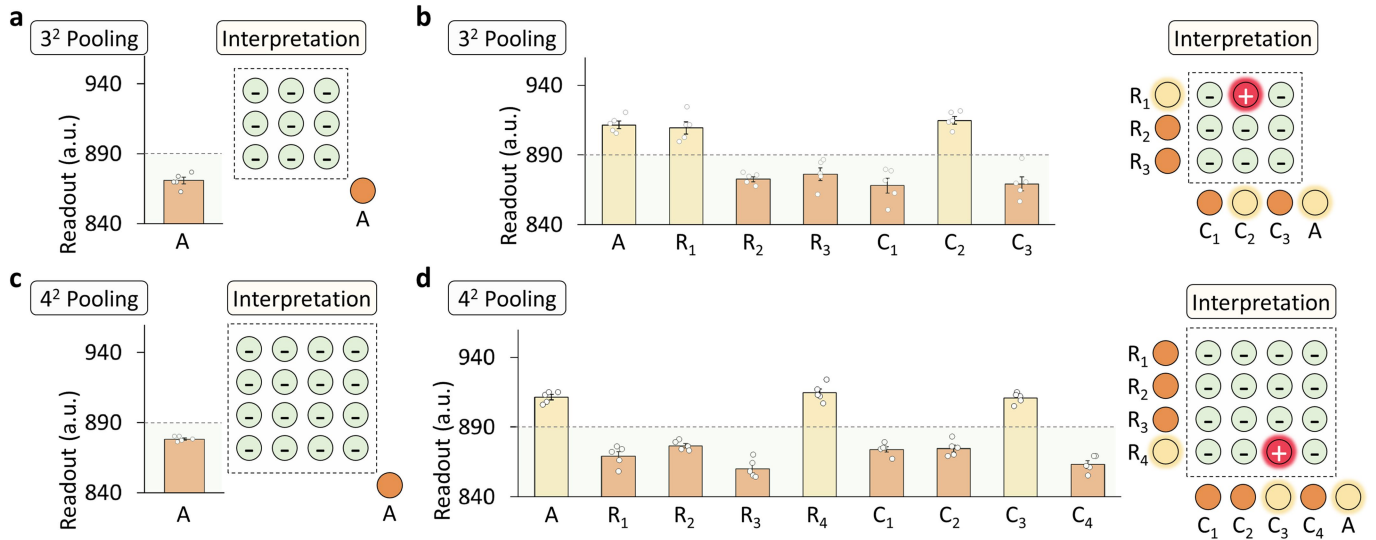
Extended Data Fig. 10 | Pooled testing using 100 nL sample volumes.
a, b, Readouts obtained from ferrobotic pooled testing of two groups of 9 clinical samples using the 32 pooling chip. The negative assay A response indicated no infected sample was present among the first group of samples in (**a**). The positive assay A response along with the positive assay R_1 and C_2 responses led to the identification of the infected sample (located at the 1st row/2nd column) among the second group of samples (**b**). **c, d**, Readouts obtained from ferrobotic pooled testing of two groups of 16 clinical samples using the 42 pooling chip. The negative assay A response indicated no infected sample was present among the first group of samples in (**c**). The positive assay A response along with the positive assay R_4 and C_3 responses led to the identification of the infected sample (located at the 4th row/3rd column) among the second group of samples (**d**). Error bars indicate repeated optical readings, mean values ± SE (n = 5). Assays were performed in small volume microfluidic chips (channel height: -150 μm; aliquoted sample volume: 100 nL; and reagent volume: 1.9 μL).

Corresponding author(s):   Sam Emaminejad, Dino Di Carlo

Last updated by author(s):   Mar 10, 2022

Reporting Summary

Nature Portfolio wishes to improve the reproducibility of the work that we publish. This form provides structure for consistency and transparency in reporting. For further information on Nature Portfolio policies, see our Editorial Policies and the Editorial Policy Checklist.

Statistics

For all statistical analyses, confirm that the following items are present in the figure legend, table legend, main text, or Methods section.

n/a	Confirmed	
☐	☒	The exact sample size (*n*) for each experimental group/condition, given as a discrete number and unit of measurement
☐	☒	A statement on whether measurements were taken from distinct samples or whether the same sample was measured repeatedly
☒	☐	The statistical test(s) used AND whether they are one- or two-sided *Only common tests should be described solely by name; describe more complex techniques in the Methods section.*
☒	☐	A description of all covariates tested
☒	☐	A description of any assumptions or corrections, such as tests of normality and adjustment for multiple comparisons
☐	☒	A full description of the statistical parameters including central tendency (e.g. means) or other basic estimates (e.g. regression coefficient) AND variation (e.g. standard deviation) or associated estimates of uncertainty (e.g. confidence intervals)
☒	☐	For null hypothesis testing, the test statistic (e.g. *F*, *t*, *r*) with confidence intervals, effect sizes, degrees of freedom and *P* value noted *Give P values as exact values whenever suitable.*
☒	☐	For Bayesian analysis, information on the choice of priors and Markov chain Monte Carlo settings
☒	☐	For hierarchical and complex designs, identification of the appropriate level for tests and full reporting of outcomes
☒	☐	Estimates of effect sizes (e.g. Cohen's *d*, Pearson's *r*), indicating how they were calculated

Our web collection on statistics for biologists contains articles on many of the points above.

Software and code

Policy information about availability of computer code

Data collection	Android Nano (for optical sensor readout), Plate reader Cytation 5 (for absorbance reading during RT-LAMP), Applied Biosystems 7500 Real-Time PCR Instrument (for RT-PCR signal readout), Nanodrop One (for absorbance reading of RT-LAMP reaction product)
Data analysis	Matlab (2021b) and Excel (version 2007) for data analysis and plotting

For manuscripts utilizing custom algorithms or software that are central to the research but not yet described in published literature, software must be made available to editors and reviewers. We strongly encourage code deposition in a community repository (e.g. GitHub). See the Nature Portfolio guidelines for submitting code & software for further information.

Data

Policy information about availability of data

All manuscripts must include a data availability statement. This statement should provide the following information, where applicable:

- Accession codes, unique identifiers, or web links for publicly available datasets
- A description of any restrictions on data availability
- For clinical datasets or third party data, please ensure that the statement adheres to our policy

All data needed to evaluate the findings and conclusions in the paper are present in the paper and/or Supplementary Information and can be accessed through the Open Science Framework at https://osf.io/ac9hz/?view_only=7b610238e37848faa05c89b7aa48e54a (https://doi.org/10.17605/OSF.IO/AC9HZ)

Field-specific reporting

Please select the one below that is the best fit for your research. If you are not sure, read the appropriate sections before making your selection.

☒ Life sciences ☐ Behavioural & social sciences ☐ Ecological, evolutionary & environmental sciences

For a reference copy of the document with all sections, see nature.com/documents/nr-reporting-summary-flat.pdf

Life sciences study design

All studies must disclose on these points even when the disclosure is negative.

Sample size	The generated clinical data presented in the main manuscript is based on analyzing a total of 100 clinical samples with the focus on assessing the accuracy of ferrobotic platform. 10 more samples were additionally analyzed as part of our revision efforts. The sample size is chosen to be sufficiently large to reliably assess the accuracy of our platform while illustrating the ease of analyzing a large number of samples by our platform.
Data exclusions	None.
Replication	Each clinical sample was tested by RT-PCR, ferrobotic individual/pooling testing, and off-chip RT-LAMP testing to validate the reproducibility of our platform. 1 test result discrepancy happened between RT-PCR and RT-LAMP testing, which is already included in Fig.3d.
Randomization	Not applicable. All samples were tested.
Blinding	None. The samples are provided by a co-author's lab.

Reporting for specific materials, systems and methods

We require information from authors about some types of materials, experimental systems and methods used in many studies. Here, indicate whether each material, system or method listed is relevant to your study. If you are not sure if a list item applies to your research, read the appropriate section before selecting a response.

Materials & experimental systems

n/a	Involved in the study
☒	☐ Antibodies
☒	☐ Eukaryotic cell lines
☒	☐ Palaeontology and archaeology
☒	☐ Animals and other organisms
☐	☒ Human research participants
☒	☐ Clinical data
☒	☐ Dual use research of concern

Methods

n/a	Involved in the study
☒	☐ ChIP-seq
☒	☐ Flow cytometry
☒	☐ MRI-based neuroimaging

Human research participants

Policy information about studies involving human research participants

Population characteristics	Nasopharyngeal swab samples were obtained from UCLA Health patients. Population characteristics of the human research participants are not provided as they are not expected to significantly affect the findings of this study.
Recruitment	Recruitment were performed by physicians following UCLA Health guidelines, which emphasize equitable subject recruitment.
Ethics oversight	UCLA IRB

Note that full information on the approval of the study protocol must also be provided in the manuscript.